UDK 669.017.15:691.714:621.791.725
Original scientific article/Izvirni znanstveni članek

ISSN 1580-2949
Mater. Tehnol.

THE EFFECT OF Y ON THE PERFORMANCE AND MICROSTRUCTURE OF FeCoCrNiMnTi$_{0.6}$ HIGH-ENTROPY ALLOY COATINGS

VPLIV DODATKA ITRIJA NA LASTNOSTI IN MIKROSTRUKTURO PREVLEK IZ ZLITIN Z VELIKO ENTROPIJO TIPA FeCoCrNiMnTi$_{0,6}$

**Shenhao Wang[1], Chuanwei Shi[1,*], Lingchen Kong[1], Xuan Hao[1], Zhiheng Zhu[1],
Fengyuan Guo[1], Yushuang Huo[1], Qian Su[1], Guoqiang Ren[2]**
[1]School of Materials Science and Engineering, Shandong Jianzhu University, Jinan 250101, China
[2]Standards & Metrology Research Institute, China Academy of Railway Sciences Corporation Limited , Haidian District,
Beijing100080, China

Prejem rokopisa – received: 2025-02-23; sprejem za objavo – accepted for publication: 2025-08-26

doi:10.17222/mit.2025.1405

In this study we prepared FeCoNiCrMnTi$_{0.6}$Y$_{\mathrm{Xwt\%}}$ (x=0.5, 0.75, 1, 1.25) high-entropy alloy coatings on c45 steel substrates using the laser-cladding method. The microstructure and properties of the cladding layers were investigated. The results indicated that the cladding layers exhibited good metallurgical bonding with the substrate, with the coatings comprising an FCC phase matrix accompanied by the precipitation of the Laves phase. With the addition of Y, the grain size of the coatings was gradually refined. Owing to the combined effects of grain-refinement strengthening, second-phase-precipitation strengthening, and solid-solution strengthening, the microhardness of the coatings increased, reaching up to twice that of the substrate. As the grains were refined, the wear resistance of the coatings initially increased and then decreased, with the optimal performance observed at x=1. The coatings also exhibited excellent corrosion resistance, which improved with increasing Y content.

Keywords: High-entropy alloy; laser cladding; rare earth

V članku avtorji opisujejo izdelavo prevlek iz zlitin z veliko entropijo tipa FeCoNiCrMnTi$_{0.6}$Y$_{X}$ (x=0,5, 0,75, 1,00 in 1,25) *w*/% na jekleno podlago iz jekla tipa c45 z uporabo tehnike laserskega navarjanja. Po navarjanju so avtorji ugotavljali mikrostrukture prevlek in njihove lastnosti. Rezultati raziskav so pokazali, da imajo prevleke dobro metalurško vez z jekleno podlago. Prevleke imajo ploskovno centrirano kubično strukturo matrične faze z izločki Lavesove faze. Legiranje z itrijem (Y) je postopoma udrobnilo kristalna zrna prevlek. S kombinacijo učinkov utrjevanja zaradi udrobljenja (zmanjševanja velikosti kristalnih zrn), utrjevanja zaradi izločanja sekundarne faze in utrjevanja trdne raztopine je mikrotrdota prevlek s povečevanjem dodatka itrija pomembno naraščala in dosegla dvakratno vrednost mikrotrdote podlage. Z udrobljenjem kristalnih zrn se je odpornost proti obrabi prevlek najprej povečala in nato zmanjšala. Optimalne lastnosti prevleke so avtorji dosegli pri vrednosti x=1. Izdelane prevleke so imele tudi odlično odpornost proti koroziji, ki se je postopoma izboljševala s povečevanjem vsebnosti itrija.

Ključne besede: zlitine z veliko entropijo; lasersko navarjanje; redko zemeljski elementi

1 INTRODUCTION

Yeh first introduced the concept of high-entropy alloys (HEAs).[1] HEAs are a novel type of alloy composed of five or more metallic elements mixed in atomic ratios of 5–35 % each. Due to their four core effects, HEAs exhibit excellent comprehensive properties,[2] such as high hardness, good corrosion resistance, and superior wear resistance,[3–6] making them highly promising for engineering applications.

CoCrFeMnNi-based high-entropy alloys (HEAs), also known as "Cantor" alloys,[7] have been a focal point of research and have been repeatedly verified to possess a single FCC structure.[8] CoCrFeMnNi-based HEA coatings can maintain excellent strength and toughness even in harsh environments.[9] They can also serve as intermediate layers to reduce the cracking tendency between hard HEA coatings and steel substrates.[10] Recently, researchers have focused on adding Ti to CoCrFeMnNi HEAs. Studies have shown that adding a small amount of Ti to the FCC-structured CoFeMnNi HEA results in CoFeMnNiTi$_{0.25}$ still retaining the FCC phase. However, with the further addition of Ti, the Laves phase begins to appear.[11] Due to Ti's larger atomic radius compared to other elements (Co, Cr, Fe, Ni, and Mn), adding Ti is expected to increase the lattice distortion in the CoCrFeNiMn matrix, thereby enhancing the solid-solution strengthening effect. Zhang et al.[12] used laser cladding to coat FeCoCrNiMnTi$_x$(B$_4$C)$_y$ HEAs on Q355 steel and found that FeCoCrNiMnTi$_x$ (x=0.5, 0.6, 0.8, 1.0) HEA coatings had much higher hardness than the substrate, with the optimal hardness at FeCoCrNiMnTi$_{0.6}$. This optimal hardness is attributed to the larger atomic radius of Ti, promoting lattice distortion and enhancing

---

*Corresponding author's e-mail:
shichuanwei@sdjzu.edu.cn (Chuanwei Shi)

© 2025 The Author(s). Except when otherwise noted, articles in this journal are published under the terms and conditions of the Creative Commons Attribution 4.0 International License (CC BY 4.0).

the solid-solution-strengthening effect. Besides solid-solution strengthening, the in-situ-formed TiN particles and Laves phase can improve the coating's hardness, making it approximately three times that of the 304 stainless-steel substrate.[13] Considering the solid-solution behavior of Ti and to avoid excessive intermetallic compound formation from too much Ti, the elemental ratio for this experiment was determined to be $FeCoCrNiMnTi_{0.6}$.

Rare-earth elements (REEs) possess outstanding physical properties that enhance material quality and performance. Liang et al.[14] investigated the effect of Y content on ZK60 magnesium alloy, finding that Y addition suppressed crack formation, refined grain size, and enhanced corrosion resistance. The best corrosion resistance was observed at 1 *w*/% Y. Gong et al.[15] demonstrated that adding REEs to Q420 steel castings purified the inclusions and improved the corrosion resistance. Recent studies have shown that incorporating REEs into multi-component alloys can enhance their performance by altering their microstructure. Zhang et al.[16] studied the influence of Y content on the microstructure and mechanical properties of an as-cast CoCrFeNi alloy. They observed a transition from a single FCC structure to an HS_1 ($CaCu_5$-type) phase structure upon Y addition. With increasing Y content, the $Y_{0.3}$ alloy exhibited a new HS_2 phase (Ni_3Y-type), accompanied by a continuous increase in alloy microhardness. Zhou et al.[17] investigated the impact of Y addition on the microstructure and mechanical properties of a $CrFeNi_2$ medium-entropy alloy, revealing a transformation from a single FCC structure to a dual-phase structure of FCC and HCP (YNi_5-type) phases with increasing Y content. This dual-phase strengthening promoted the hardness and compressive yield strength of $CrFeNi_2Y$. This study explores the influence of Y content on Ti-enhanced HEA performance.

The deposition of high-entropy alloy (HEA) coatings on low-cost steel substrates holds importance for enhancing HEA applications and economizing the consumption of expensive elements in HEAs such as Co, Cr, and Ni. Currently, research on the laser cladding of HEA coatings containing REEs on common low-carbon steel surfaces is limited. In this study, a $FeCoNiCrMnTi_{0.6}Y_X$ (*x*=0.5 *w*/%, 0.75 *w*/%, 1 *w*/%, 1.25 *w*/%) high-entropy alloy coating was laser clad onto the surface of c45 steel, with Fe derived from the c45 steel itself. The microstructure and corrosion resistance of the coatings were investigated and analyzed.

2 EXPERIMENTAL PROCEDURE

High-purity non-spherical powders of Co, Cr, Ni, Mn, Ti, and Y (purity > 99.5 *w*/%) with particle sizes ranging from 50 μm to 150 μm were selected to prepare coatings on the surface of c45 steel using laser cladding. This study aims to investigate the effects of different Y contents on the microstructure and properties of FeCoNiCrMnTi0.6 high-entropy alloy (HEA) coatings and their underlying mechanisms. Based on prior experiments with the stoichiometric ratio of FeCoNiCrMnTi0.6, the required powder weight for different Y concentrations (0.5 *w*/%, 0.75 *w*/%, 1 *w*/%, and 1.25 *w*/%) was calculated. After accurately weighing 30 g of the powder mixture (as shown in **Table 1**), the powders were mixed for 12 h in a V-shaped mixer to ensure uniformity. The metal powders were then evenly applied to the surface of the c45 steel (as shown in **Table 2**) using the adhesive property of water glass (primarily composed of Na_2SiO_3), with a coating thickness of 1.5 mm above the steel surface. Laser cladding experiments were conducted using a YLS-10000 laser processing system under high-purity argon-gas protection. Specific process parameters are detailed in **Table 3**.

The phase structure of the materials was analyzed using Cu-Kα X-ray diffraction (XRD) with operating conditions of 40 kV, 40 mA, and a scanning rate of 5°/min. The microstructure of the samples was examined using a JEOL-7800F scanning electron microscope (SEM). The elemental distribution was characterized using energy-dispersive spectroscopy (EDS). The grains on the surface of the coating were observed using a 3D ultra-depth-of-field digital microscope (VHX-5000) and

Table 1: Powder weight ratios (g)

Sample	Co	Cr	Mn	Ni	Ti	Y
x=0.5	13.981	12.256	12.949	13.833	6.771	0.3
x=0.75	13.956	12.225	12.917	13.799	6.754	0.45
x=1	13.821	12.194	12.884	13.764	6.737	0.6
x=1.25	13.786	12.13	12.851	13.729	6.72	0.75

Table 2: Chemical composition of c45 steel

Element	Fe	C	Si	Mn	S	P
Percentage	Bal	0.42% – 0.50%	0.17% – 0.37%	0.50% – 0.80%	≤0.035%	≤0.035%

Table 3: Laser Process Parameters

Laser power	Scanning speed	Spot diameter	Out-of-focus amount	Overlap rate	Protective gas rate
0.9 kW	15 mm/s	1.5mm	35 mm	30%	15 L/min

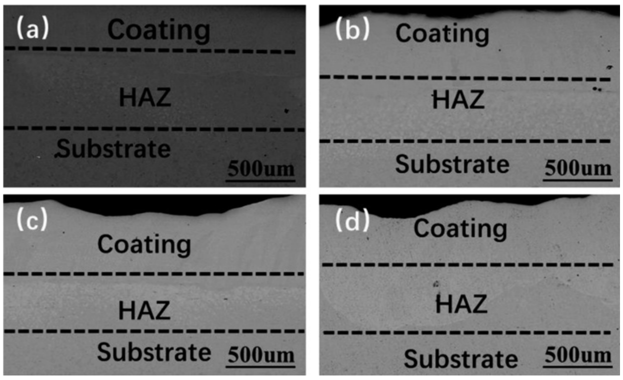

Figure 1: Cross section morphology of HEA coating: a) FeCoNiCrMnTi$_{0.6}$Y$_{0.5\ w/\%}$; b) FeCoNiCrMnTi$_{0.6}$Y$_{0.75\ w/\%}$; c) FeCoNiCrMnTi$_{0.6}$Y$_{1\ w/\%}$; d) FeCoNiCrMnTi$_{0.6}$Y$_{1.25\ w/\%}$

the grain size was calculated using ImageJ software. The microhardness of the coatings was measured using a Vickers hardness tester (HXD-1000TMC/LCD) under a load of 200 g for 10 s. The friction and wear of the coatings were evaluated using a reciprocating wear tester (HSR-2M) with an 8-mm stroke length, 20-min duration, and a YG6 hard alloy counterpart. Electrochemical tests of the samples and c45 steel were conducted using a Gamry Interface 1000E electrochemical workstation at room temperature in a 3.5 *w*/% NaCl solution. Potentiodynamic polarization curves were recorded at a scan rate of 0.5 mV/s over a potential range of 0.5 V to 1.8 V vs. open-circuit potential. Electrochemical impedance spectroscopy (EIS) curves were analyzed using ZsimpWin data-analysis software (AMETEK Scientific Instruments, Inc., USA).

3 RESULTS AND DISCUSSION

(1) Cross-Section Morphology

Figure 1 shows the cross-sectional morphology of the HEA coatings, demonstrating good metallurgical bonding between the HEA and c45 steel substrate. The coatings exhibit uniform thickness, with an average thickness of approximately 0.6 mm.

Figure 2 displays the optical microstructure of the HEA coatings. Both *x*=0.5 and *x*=0.75 samples exhibit dendritic structures, while the x=1 sample predominantly consists of fine equiaxed grains. The *x*=1.25 sample exhibits a mixture of dendritic and cellular structures. As

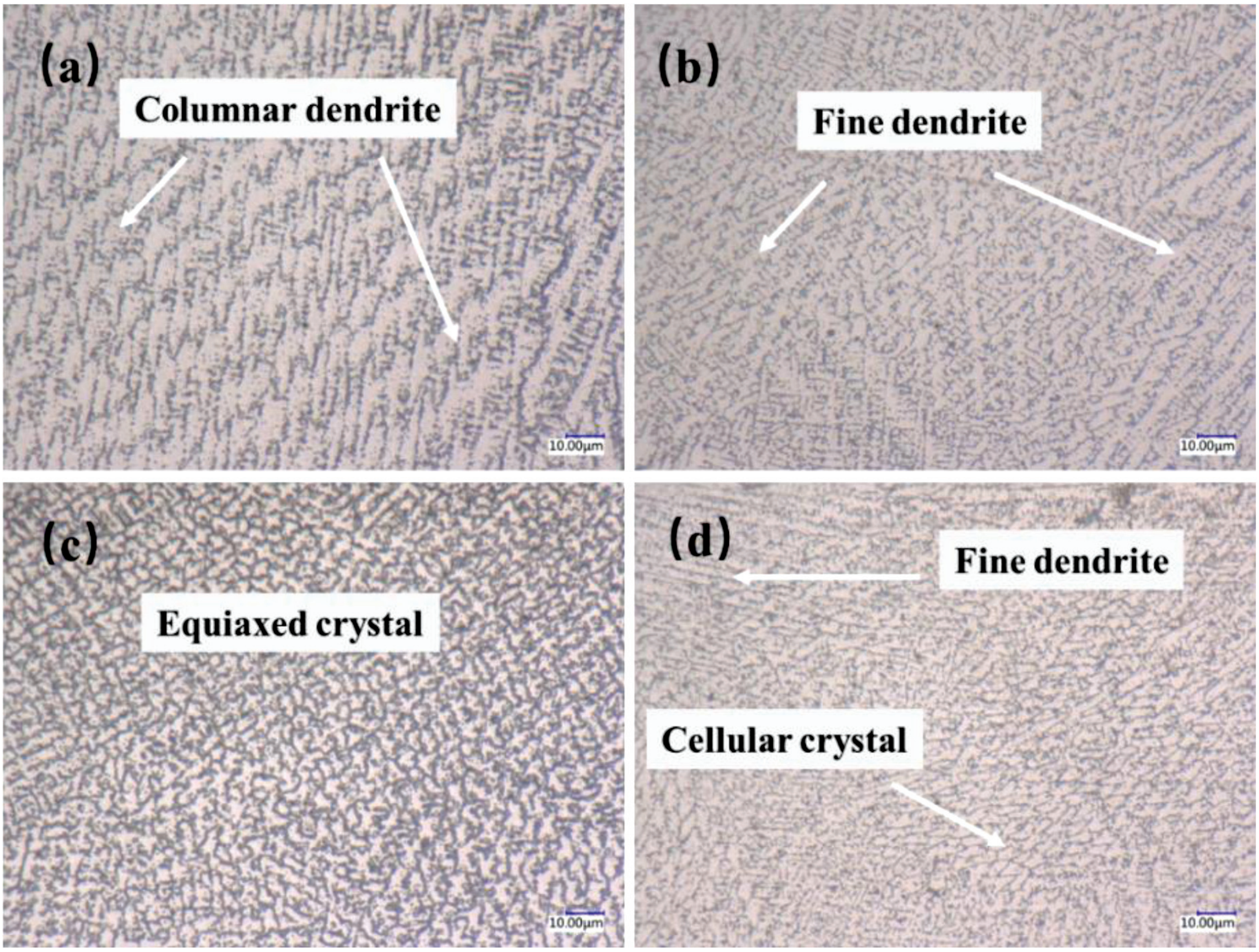

Figure 2: optical microstructure of HEA coatings: a) FeCoNiCrMnTi$_{0.6}$Y$_{0.5\ w/\%}$, b) FeCoNiCrMnTi$_{0.6}$Y$_{0.75\ w/\%}$, c) FeCoNiCrMnTi$_{0.6}$Y$_{1\ w/\%}$, d) FeCoNiCrMnTi$_{0.6}$Y$_{1.25\ w/\%}$

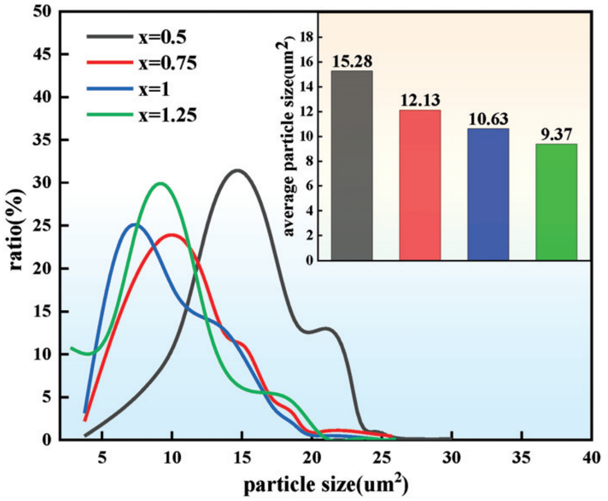

Figure 3: Grain distribution map of the HEA coatings

shown in **Figure 3**, an increase in Y content results in smaller grain sizes, with the finest grains observed in the x=1.25 sample, where the average grain size measures 9.37 μm². This phenomenon is attributed to the accumulation of Y at the solid-liquid interface during solidification, which enlarges the undercooling zone and accelerates nucleation rates.[18]

(2) Microstructure

Table 4: Element parameters

Element	Atomic number	melting point (°C)	Atomic radius	Relative atomic mass
Y	39	1522	2.27	88.91
Fe	26	1539	1.72	55.85
Co	27	1493	1.67	58.93
Ni	28	1455	1.62	58.69
Cr	24	1863	1.85	52.00
Mn	25	1244	1.79	54.94
Ti	22	1668	1.44	47.87

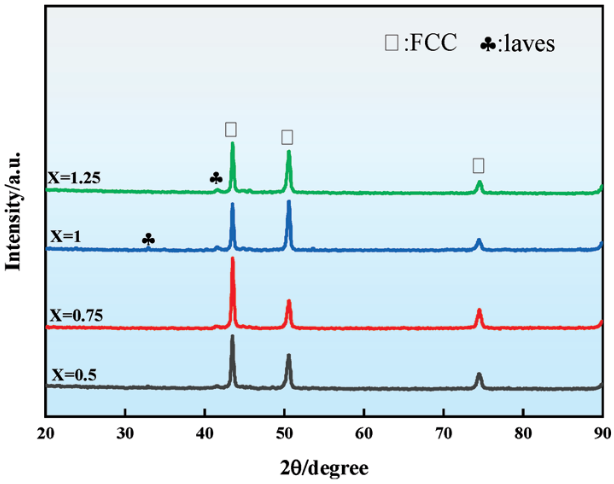

Figure 4: XRD spectra of the HEA coatings

Figure 4 shows the XRD patterns of the FeCoCrNiMnTi$_{0.6}$Y$_X$ coatings. In all samples, both FCC and Laves phases (mainly composed of YNi$_5$ and Ti) are observed. The presence of Laves phase, where Ti precipitates along with Y as a stabilizer of the hexagonal close-packed (HCP) structure,[19] is notable. It is important to note that the peak intensity of the Laves phase is lower than that of the FCC phase, indicating that the FCC phase remains predominant.

Table 5: Mixing enthalpy of coating elements

Element	Fe	Co	Ni	Cr	Mn	Ti	Y
Fe	–	–1	–2	–1	0	–17	–1
Co	–	–	0	–4	–5	–28	–22
Ni	–	–	–	–7	–8	–35	–31
Cr	–	–	–	–	2	–7	11
Mn	–	–	–	–	–	–8	–1
Ti	–	–	–	–	–	–	15
Y	–	–	–	–	–	–	–

From a thermodynamic perspective, the composition of HEAs can be elucidated using the Miedema model, which calculates the chemical mixing enthalpy of atomic pairs in the coating,[20] as shown in **Table 5**. The mixing entropy increases with the number of elements in the alloy, promoting the formation of solid solutions. Yang[21] proposed Ω to assess the formation capability of solid solutions. The mixing enthalpy (ΔH_{mix}), mixing entropy (ΔS_{mix}), and atomic size difference (δ) of HEAs can be predicted using the following formulas:[22,23]

$$\Delta S_{\mathrm{mix}} = -R\sum c_i \ln c_i \tag{1}$$

$$\Delta H_{\mathrm{mix}} = \sum_{i,j=1,i\neq j}^{n} 4\Delta H_{\mathrm{mix}}^{\mathrm{AB}} c_i c_j \tag{2}$$

$$\delta = \sqrt{\sum_{i=1}^{n} c_i \left(1-\frac{r_i}{\bar{r}}\right)^2} \tag{3}$$

In the equations, R denotes the gas constant (8.314 J/(K·mol)); c_i represents the atomic fraction of the i element. n denotes the number of elements; $\Delta H_{\mathrm{mix}}AB$ represents the mixing enthalpy of the binary alloy (see **Table 5**); $\bar{r}$ denotes the average atomic radius of the elements. r_i represents the atomic radius of the i element (see **Table 4**).

Table 6: Thermodynamic parameters calculated for FeCoNiCrMnTi$_{0.6}$Y$_{1\mathrm{wt}\%}$

sample	ΔS_{mix} (J/mol K)	ΔH_{mix} (J/mol K)	δ (%)	K (kJ/mm^{-2})
X=0.5	14.86	–20.02	7.65	0.055
X=0.75	14.91	–20.15	7.74	0.055
X=1	14.97	–20.18	7.86	0.055
X=1.25	15.03	–20.24	7.96	0.055

Typically, solid-solution formation is more favorable when $11 \leq \Delta S_{\mathrm{mix}} \leq 17.5$ J/mol·K, $-22 \leq \Delta H_{\mathrm{mix}} \leq 7$ KJ/mol and $\delta \leq 6.6$.[20] As per the calculations based on **Table 4**

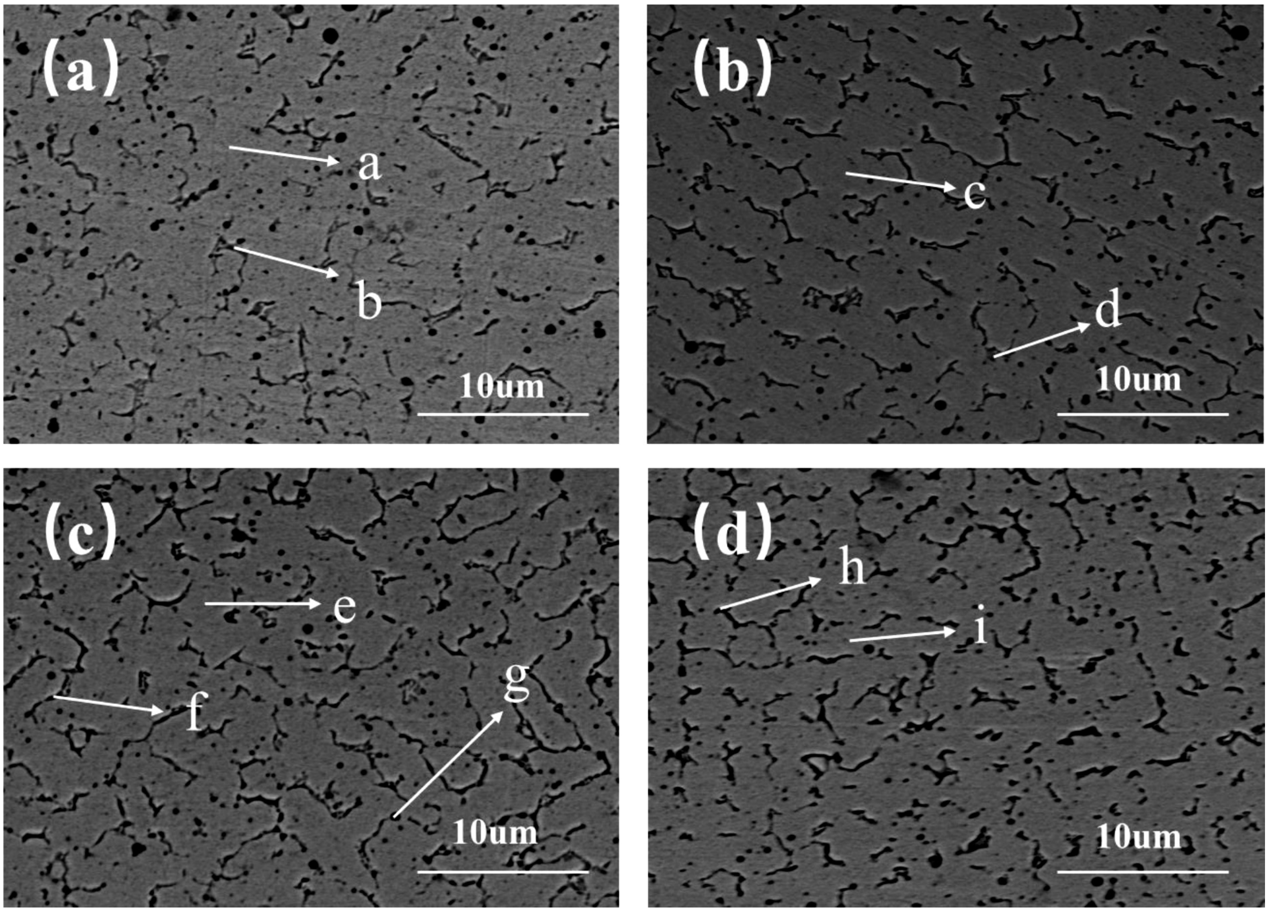

Figure 5: SEM image of the HEA coating: a) FeCoNiCrMnTi$_{0.6}$Y$_{0.5\,w/\%}$, b) FeCoNiCrMnTi$_{0.6}$Y$_{0.75\,w/\%}$, c) FeCoNiCrMnTi$_{0.6}$Y$_{1\,w/\%}$, d) FeCoNiCrMnTi$_{0.6}$Y$_{1.25\,w/\%}$

and the aforementioned equations, the results presented in **Table 6** are within this specified range, indicating that the alloy element design in this study facilitates solid-solution formation.

During laser cladding, the high cooling rate of the melt pool suppresses the formation of intermetallic compounds when this rate exceeds the atomic diffusion rate of these compounds within the superlattice, thereby promoting the formation of solid solutions.[22] Hence, the influence on the phase composition can be evaluated using the laser-energy input parameter K, as shown in **Table 6**.

$$K=\frac{P}{D\cdot v} \tag{4}$$

In the equation, P represents the laser power, D denotes the diameter of the laser beam spot, and v stands for the scanning speed.

Studies have shown that higher K values lead to increased dilution rates and deteriorate the coating performance, resulting in reduced cooling rates of the molten pool and a propensity for intermetallic compound formation.[19] Therefore, the appropriate range for K should be controlled between 0.04 and 0.14. In this study, a K value of 0.055 indicates that laser cladding suppresses the intermetallic-compound formation and promotes solid-solution formation.

From a thermodynamic perspective, when the mixing enthalpy is negative, the greater its absolute value, the more likely intermetallic compounds are formed; conversely, segregation is more likely. Only when the mixing enthalpy approaches zero does it tend to favor

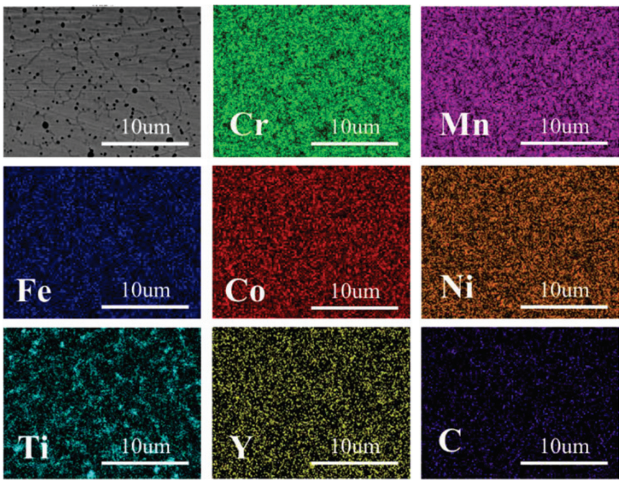

Figure 6: SEM surface scanning element distribution

Table 7: EDS Point Scan Results of HEA Coating

Sample	Point	Fe	Co	Ni	Cr	Mn	Ti	Y	C
X=0.5	a	22.8	20.4	18.3	20.3	14.1	1.9	0.2	2.1
	b	12.8	16.8	23.5	16.5	16.5	9.6	0.9	3.4
X=0.75	c	21.5	20.1	17.7	19.5	16.0	2.9	0.3	2.0
	d	15.1	16.2	21.1	17.3	16.2	9.0	0.8	4.3
X=1	e	24.8	23.7	17.3	13.6	15.4	2.3	0.4	2.4
	f	10.1	16.9	26.7	16.2	15.3	9.3	1.0	4.5
	g	9.7	9.6	9.2	10.1	10.6	31.9	0.2	18.7
X=1.25	h	24.5	19.9	17.3	19.7	12.6	1.3	0.6	4.1
	i	16.1	15.6	22.8	14.6	16.4	9.6	1.2	3.8

solid-solution formation.[21] The absolute values of the mixing enthalpy for Y and Ni are larger, making them more prone to intermetallic compound formation.

SEM images of HEA with varying Y content are depicted in **Figure 5** and **Figure 6**, while **Table 7** presents the EDS point scan results. Combined analysis of SEM images and XRD reveals that the coating primarily consists of two phases: a main phase in lighter areas and a darker reticulated precipitate phase. Additionally, there exists a minor amount of black precipitate phase, with EDS results at point G indicating higher Ti and C content, confirming it as in-situ-formed TiC ceramic reinforcement phase, albeit not prominently detected in XRD due to its low concentration. Regions with widespread lighter areas such as zones a, c, e, and h exhibit uniform distribution and content of Fe, Co, Cr, Ni, and Mn elements, consistent with the composition of the FCC phase in FeCoCrNiMn-based HEAs.[24] Therefore, these areas are identified as the FCC solid solution of FeCoCrNiMn. Conversely, point-scan results from regions b, d, f, and i show higher proportions of Y and Ni, confirming the presence of Y-Ni compounds at grain boundaries, identified as laves phase enriched in Y, Ni, and Ti, consistent with XRD findings. Moreover, with increasing Y content, the Y content stabilizes in the FCC regions (light areas) of each sample, while Ni content decreases continuously, indicating increased segregation of Y and Ni elements at grain boundaries.

(3) Hardness and wear resistance

Figure 7 illustrates the microhardness of the HEA coatings, showing an increase in average hardness with increasing Y content. The hardness peaks at x=1.25 *w*/% Y, reaching more than double that of the c45 steel substrate. The addition of Y promotes grain refinement, increasing the number of grain boundaries that hinder dislocation movement and thereby enhancing coating hardness through grain-boundary strengthening. Moreover, with increasing Y content, the proportion of HCP phase increases. Compared to the FCC phase, the Laves phase exhibits higher hardness, and its role in second-phase strengthening contributes to the overall hardness of the alloy coating.

Furthermore, due to the larger atomic radii of Y and Ti compared to Fe, Co, Cr, Ni, and Mn, their solubility in the matrix leads to lattice distortion, increasing the resistance to dislocation motion and consequently enhancing the coating's hardness. Additionally, the formation of small amounts of in-situ TiC contributes to grain refinement and second-phase strengthening effects.[25] Collectively, these mechanisms—grain boundary strengthening, second-phase strengthening, and solid solution strength-

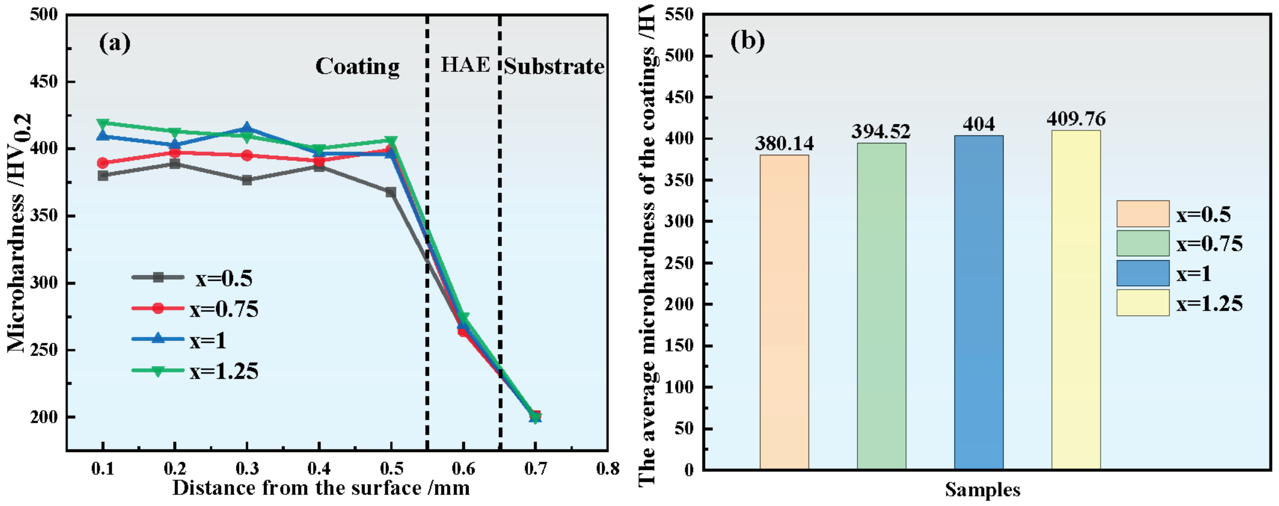

Figure 7: Coating Microhardness

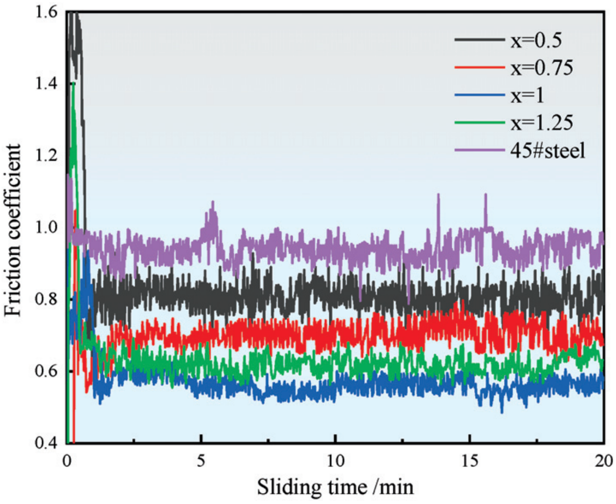

Figure 8: Friction coefficient curves of HEA coatings with c45 Steel

ening—result in a coating hardness exceeding that of c45 steel.

As shown in **Figure 8**, during the steady wear stage, the average friction coefficients of the coatings and 45 steel were 0.81, 0.70, 0.57, 0.62, and 0.94, respectively. With increasing Y content, the wear resistance initially increased and then decreased, reaching its optimum at x=1. This improvement in wear resistance is attributed to grain refinement, which enhances the coating's hardness and plasticity, increases grain-boundary density, and impedes dislocation movement. Generally, harder materials have lower friction coefficients and higher wear resistance.[26] Additionally, the formation of dendrites reduces the coating's strength and toughness, increasing brittleness and thus reducing wear resistance. The superior wear resistance of the x=1 sample is due to the predominance of equiaxed grains.[27]

To determine the wear mechanisms of the coatings, scanning electron microscopy (SEM) was used to observe the wear morphology, as shown in **Figure 8**. In (a), the large spalling pits are related to reduced hardness and decreased micro-cutting resistance, indicating that the primary wear mechanism is adhesive wear. With increasing Y content, the wear mechanism gradually shifts to abrasive wear, as evidenced by the plowing grooves observed in (b), (c), and (d). The hard particles within the coating are the main cause of these plowing grooves, and the occurrence of abrasive wear in the coating highlights its superior wear resistance.

(4) Corrosion Performance

As shown in **Figure 9**, the potentiodynamic polarization curves of the FeCoNiCrMnTi0.6YX% coatings and c45 steel in a 3.5 % NaCl solution are presented. From the anodic polarization curves, it can be observed that all the curves, except for that of c45 steel, exhibit a passivation trend, indicating the occurrence of

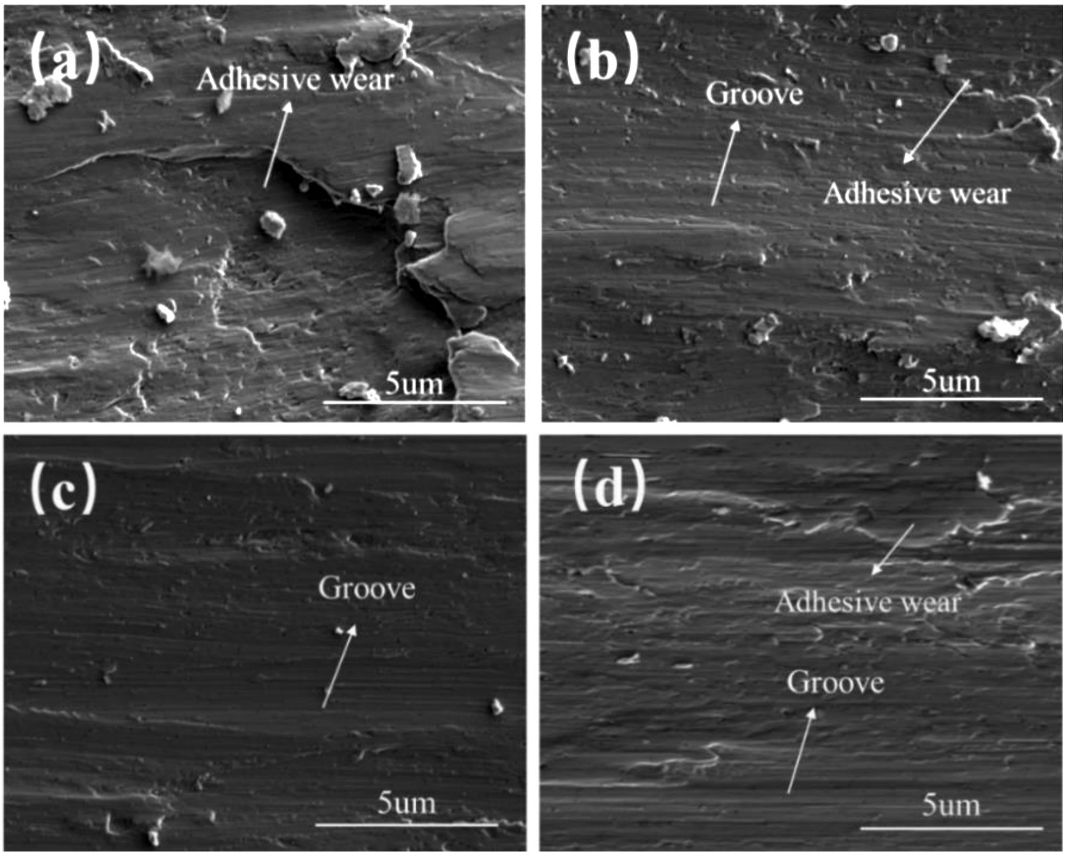

Figure 9: Wear morphology of HEA coatings: a) x = 0.5; b) x = 0.75; c) x = 1; d) x = 1.25

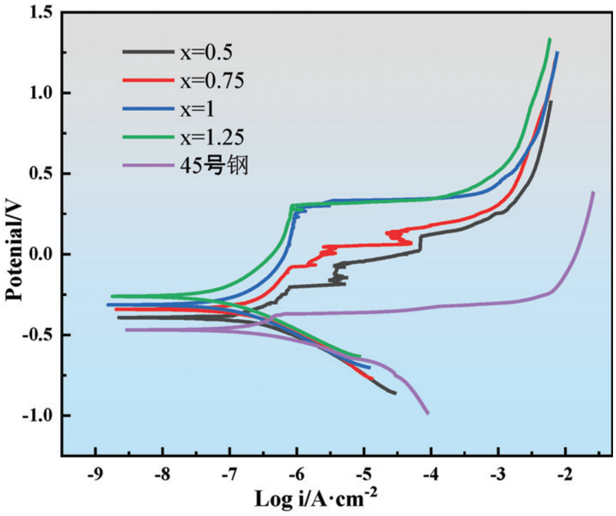

Figure 10: Potentiodynamic polarization curves of HEA coatings and 45 #steel

passivation. Figure 11 shows the equivalent circuit diagram of the passivation phenomenon. When the Ti content in the coating is higher, a stable passive film is typically formed.[28] The cathodic polarization curves represent hydrogen-evolution processes,[29] and the similar shapes of the cathodic polarization curves after Y addition suggest minimal influence of Y content on the cathodic current density. The corrosion potentials (E_{corr}), corrosion current densities (i_{corr}), anodic Tafel slopes (β_a), and cathodic Tafel slopes (β_c) extrapolated from the Tafel lines are listed in **Table 8**. Compared to 45 steel, each coating exhibits higher corrosion potentials and lower corrosion current densities. The i_{corr} values of the coatings are 9.25 %, 7.79 %, 4.67 %, and 2.55 % of that of 45 steel, respectively, with the corrosion resistance of the coatings improving progressively with increasing Y content.

Table 8: Corrosion kinetic parameters of coatings and 45 steel

Sample	E_{corr}(V)	i_{corr}(A·cm^2	β_a(mV·dec^{-1})	β_c(mV·dec^{-1})
X=0.5	–0.682	1.50605E-07	0.1795	–0.15689
X=0.75	–0.327	1.44642E-07	0.2694	–0.1483
X=1	–0.322	7.42951E-08	0.2132	–0.1492
X=1.25	–0.318	4.7819E-08	0.2087	–0.1394
c45steel	–0.306	1.36574E-08	0.0199	–0.1107

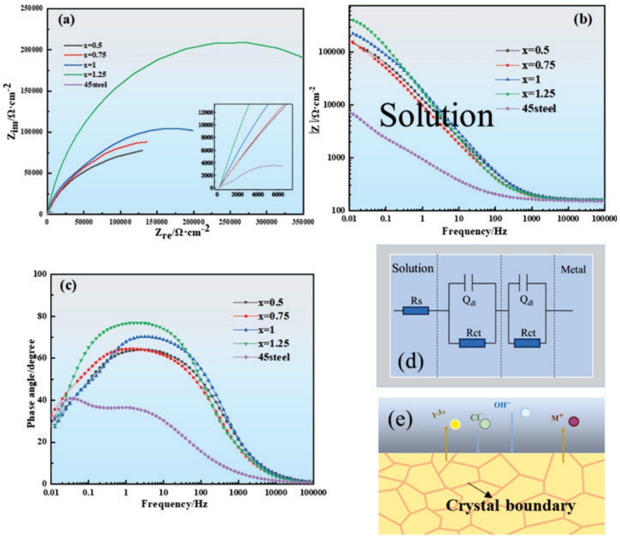

Figure 11: EIS curves of HEA coating and c45 steel: a) Nyquist plot; b) The relationship between impedance amplitude and phase angle of c) bad plot and frequency; d) R_s ($Q_{dl}R_{ct}$)(Q_fR_f) Corrosion Circuit Diagram; (e)Electrochemical corrosion mechanism diagram of the coating

The EIS fitting results are presented in **Table 9**. Rct denotes the charge-transfer resistance, and it is evident that the R_{ct} values of all the coatings are higher than that of 45 steel. Generally, higher R_{ct} values indicate better corrosion resistance,[30] consistent with the polarization curve results, suggesting that the addition of Y improves the corrosion resistance of the coatings. Song et al.[31] suggested that the continuous phase along the grain boundaries can prevent corrosion from diffusing from one grain to another. Pardo et al.[32] and Shuai et al.[33] argued that the presence of continuous networked precipitates can inhibit corrosion. As shown in **Figure 12**, an SEM analysis reveals the presence of a dense networked precipitate phase containing Y, Ni, and Ti in the coating. The continuous network distribution of the precipitate phase at the grain boundaries is more conducive to the stability and integrity of the corrosion product film. This reduces the surface area of the active cathode and the occurrence of pitting, thereby slowing down the diffusion rate of the metal cations and decreasing the tendency for localized corrosion in the alloy. To some extent, this improves the alloy's corrosion resistance. Thus, Y elements likely enhance the corrosion resistance of the coatings by

Table 9: EIS fitting parameters

Sample	R_S(Ω·cm^{-2})	Q_{dl}		R_f(Ω·cm^{-2})	Q_{dl}		R_{ct}(Ω·cm^{-2})
		Y_{dl}	n_1		Y_{dl}	n_1	
X=0.5	158.2	4.772E-005	0.8	2.113E004	3.141E-005	0.7	2.459E004
X=0.75	154	3.385E-005	0.71	2.686E004	2.578E-005	0.92	2.685E004
X=1	158.8	2.622E-005	1	2.955E004	1.825E-005	0.76	3.391E004
X=1.25	158.4	1.041E-005	0.89	3102E004	1.109E-005	0.88	4.933E004
45steel	150.4	0.0003798	0.55	–	–	–	6253

forming continuous network-like precipitates that hinder corrosion diffusion.

4 CONCLUSION

In this study, a FeCoNiCrMnTi$_{0.6}$Y$_x$ (x = 0.5 *w*/%, 0.75 *w*/%, 1 *w*/%, 1.25 *w*/%) high-entropy alloy coating was deposited on the surface of 45 steel. The phase structure, microstructure, hardness, and corrosion resistance of the deposited coatings were investigated. The following conclusions could be drawn:

(1) The coating exhibited good metallurgical bonding with 45 steel. With increasing Y content, the grain size of the coating continuously decreased, reaching a minimum of 9.37 µm^2. The coatings featured an FCC matrix phase accompanied by Laves phase precipitation.

(2) The hardness of the coatings significantly increased due to grain refinement strengthening, second-phase reinforcement, and solid solution strengthening effects, reaching up to twice that of the 45 steel substrate. As grain size decreased, the wear resistance of the coatings initially increased and then decreased, with optimal performance observed at x=1. The predominant wear mechanisms were abrasive wear and adhesive wear.

(3) Compared to 45 steel, the coatings exhibited excellent corrosion resistance, which improved progressively with increasing Y content. This enhancement in corrosion resistance could be attributed to the continuous network-like precipitates formed by Y elements, which effectively hindered the diffusion of corrosion products and thereby promoted the corrosion resistance of the coatings.

Acknowledgements

The authors sincerely thank Professor Yuanbin Zhang for his guidance on research ideas and Dr. Shushuai Liu for providing an excellent experimental environment. This work was conducted at the School of Materials Science and Engineering, Shandong Jianzhu University. Special thanks to Shandong University and the Standards & Metrology Research Institute, China Academy of Railway Sciences Corporation Limited, for their support with experimental equipment, which facilitated this research.

Author Contributions

Shenhao Wang handled data processing and manuscript writing.Chuanwei Shi provided the experimental ideas, while Shenhao Wang, Lingchen Kong, Xuan Hao, Zhiheng Zhu, and Fengyuan Guo participated in the laser cladding, electrochemical experiments, and wear tests. Yushuang Huo, Qian Su, and Guoqiang Ren provided technical guidance during the experimental process.

Data and code availability

The data will be made available on request.

Conflict of Interest

The authors declare that they have no conflict of interest

Acknowledgement

This work was financially supported by the projects from the Shandong Provincial Department of Science and Technology, China (Grant Nos. 2024TSGC0296, 2024TSGC0066).

5 REFERENCE

[1] J. W. Yeh, S. K. Chen, S. J. Lin, et al., Nanostructured high-entropy alloys with multiple principal elements: novel alloy design concepts and outcomes, Advanced engineering materials, 6 (**2004**) 5, 299–303

[2] Y. Zhang, T. T. Zuo, Z. Tang, et al., Microstructures and properties of high-entropy alloys, Progress in Materials Science, 61 (**2014**) 1–93

[3] M. Qi, Z. Wei, S. Chuanwei, et al., Effect of synergistic variation in Ti and Zr elements on the microstructure and properties of laser cladding AlCoCrFeNi high-entropy alloy coatings, Materials Characterization, 205 (2023)

[4] Z. Wei, L. Zhen, S. Chenxiao, et al., Al and Mo synergistic enhancement of CoCrFeNi high-entropy alloy laser cladding layer, Journal of Materials Research and Technology, 28 (**2024**) 2572–2581

[5] K. Kedong, Z. Wei, L. Zhen, et al., High-temperature oxidation behavior and corrosion resistance of in-situ TiC and Mo reinforced AlCoCrFeNi-based high entropy alloy coatings by laser cladding, Ceramics International, 49 (**2023**) 6, 10151–10164

[6] Z. Li, W. Zhao, K. Yu, et al., Effect of Y2O3 on microstructure and properties of CoCrFeNiTiNb high entropy alloy coating on Ti–6Al–4V surface by laser cladding, Journal of Rare Earths, 42 (**2024**) 3, 586–599

[7] B. Cantor, Multicomponent high-entropy Cantor alloys, Progress in Materials Science, 120 (**2020**) 100754

[8] Z. Qi, W. Qin, H. Bin, et al., Comparative studies on microstructure and properties of CoCrFeMnNi high entropy alloy coatings fabricated by high-speed laser cladding and normal laser cladding, Journal of Alloys and Compounds, 947 (2023)

[9] H. Hongyu, L. Yang, W. Yonggang, et al., Temperature-dependent dynamic compressive properties and failure mechanisms of the additively manufactured CoCrFeMnNi high entropy alloy, Materials Design, 224 (2022)

[10] C. Yangchuan, S. Da, C. Yan, et al., Effect of CoCrFeMnNi transition cladding layer on crack resistance of CoCrFeMnNi + x(TiC) composite cladding layer, Materials Letters, 304 (2021)

[11] P. Cui, Y. Ma, L. Zhang, et al., Effect of Ti on microstructures and mechanical properties of high entropy alloys based on CoFeMnNi system, Materials Science Engineering A, 737 (**2018**) 198–204

[12] Y. Zhang, P. Zhang, H. Liu, et al., The effect of Ti and B4C on the microstructure and properties of the laser clad FeCoCrNiMn based high entropy alloy coating, Surface Coatings Technology, 441 (2022)

[13] L. S.S., Z. M., Z. G.L., et al., Microstructure and properties of ceramic particle reinforced FeCoNiCrMnTi high entropy alloy laser cladding coating, Intermetallics, 140 (2022)

[14] L. Jingwei, W. Shibo, L. Bingwei, et al., Microstructure and corrosion behavior of Y-modified ZK60 Mg alloy prepared by laser powder bed fusion, Corrosion Science, 211 (2023)

[15] G. Weiwei, Y. Bingkun, C. Hao, et al., Effects of Ce-La rare earth microalloying on the microstructure and corrosion characteristics of Q420 high-strength steel, International Journal of Electrochemical Science, 18 (**2023**) 9

[16] L. Zhang, M. Zhang, Z. Zhou, et al., Effects of rare-earth element, Y, additions on the microstructure and mechanical properties of CoCrFeNi high entropy alloy, Materials Science Engineering A, 725 (**2018**) 437–446

[17] Z. Haiping, M. Jingxiang, J. Hui, et al., Effect of rare-earth element Y addition on microstructure and mechanical properties of CrFeNi2 medium entropy alloy, Intermetallics, 163 (2023)

[18] J. Wang, S. Gao, P. Song, et al., Effects of phase composition on the mechanical properties and damping capacities of as-extruded Mg–Zn–Y–Zr alloys, Journal of Alloys and Compounds, 509 (**2011**) 34, 8567–8572

[19] L. Guénée, K. Yvon, Structure stability maps for intermetallic AB5 compounds, Journal of Alloys and Compounds, 356–357 (**2003**) 114–119

[20] A. Takeuchi, A. Inoue, Classification of Bulk Metallic Glasses by Atomic Size Difference, Heat of Mixing and Period of Constituent Elements and Its Application to Characterization of the Main Alloying Element, MATERIALS TRANSACTIONS, 46 (**2005**) 12, 2817–2829

[21] X. Yang, Y. Zhang, Prediction of high-entropy stabilized solid-solution in multi-component alloys, Materials Chemistry and Physics, 132 (**2012**) 2–3, 233–238

[22] Y. Juan, J. Li, Y. Jiang, et al., Modified criterions for phase prediction in the multi-component laser-clad coatings and investigations into microstructural evolution/wear resistance of FeCrCoNiAlMox laser-clad coatings, Applied Surface Science, 465 (**2019**) 700–714

[23] S. GUO, C. LIU, Phase stability in high entropy alloys: Formation of solid-solution phase or amorphous phase, Progress in Natural Science: Materials International, 21 (**2011**) 6, 433–446

[24] B. Cantor, I. Chang, P. Knight, et al., Microstructural development in equiatomic multicomponent alloys, Materials Science Engineering A, 375–377 (**2004**) 213–218

[25] W. H., W. L., Z. S., et al., Corrosion and cavitation erosion behaviors of laser clad FeNiCoCr high-entropy alloy coatings with different types of TiC reinforcement, Surface Coatings Technology, 471 (2023)

[26] Z. Jie, H. Yanfei, C. Zhenbing, et al., Preparation of NiCrBSi-WC/Co coatings by stable magnetic field assisted supersonic plasma spraying and its wear resistance mechanism, Materials Characterization, 194 (2022)

[27] Z. Xinyu, J. Weiju, M. Xiaonan, Effect of microstructure on the tensile properties and impact toughness of TC21G titanium alloy, Materials Characterization, (2022) 111752

[28] J. Liu, H. Liu, P. Chen, et al., Microstructural characterization and corrosion behaviour of AlCoCrFeNiTix high-entropy alloy coatings fabricated by laser cladding, Surface Coatings Technology, 361 (2019) 63–74

[29] C. Zhong, M. He, L. Liu, et al., Formation of an aluminum-alloyed coating on AZ91D magnesium alloy in molten salts at lower temperature, Surface Coatings Technology, 205 (**2010**) 7, 2412–2418

[30] W. Qi, W. Wang, X. Yang, et al., Effect of Zr on phase separation, mechanical and corrosion behavior of heterogeneous CoCrFeNiZrx high-etropy alloy, Journal of Materials Science Technology, 109 (**2022**) 14, 76–85

[31] G. Song, A. Atrens, X. Wu, B. Zhang, Corrosion behaviour of AZ21, AZ501 and AZ91 in sodium chloride, Corrosion Science, 40 (**1998**) 10, 1769–1791

[32] A. Pardo, M. Merino, A. Coy, et al., Influence of microstructure and composition on the corrosion behaviour of Mg/Al alloys in chloride media, Electrochimica Acta, 53 (**2008**) 27, 7890–7902

[33] S. Cijun, Y. Youwen, P. Shuping, et al., Nd-induced honeycomb structure of intermetallic phase enhances the corrosion resistance of Mg alloys for bone implants, Journal of materials science. Materials in medicine, 28 (**2017**) 9, 130